

Change detection in urban areas by object-based analysis and on-the-fly comparison of multi-view ALS data

Marcus Hebel^a, Michael Arens^a, Uwe Stilla^b

^a*Fraunhofer Institute of Optronics, System Technologies, and Image Exploitation IOSB,
76275 Ettlingen, Germany, {marcus.hebel, michael.arens}@iosb.fraunhofer.de, Phone: +49-7243-992-323*

^b*Photogrammetry and Remote Sensing, Technische Universität München,
80290 München, Germany, stilla@tum.de*

Abstract

The use of helicopters as a sensor platform offers flexible fields of application due to adaptable flying speed at low flight levels. Modern helicopters are equipped with radar altimeters, inertial navigation systems (INS), forward-looking cameras and even laser scanners for automatic obstacle avoidance. If the 3D geometry of the terrain is already available, the analysis of airborne laser scanner (ALS) measurements may also be used for terrain-referenced navigation and change detection. In this paper, we present a framework for on-the-fly comparison of current ALS data to given reference data of an urban area. In contrast to classical difference methods, our approach extends the concept of occupancy grids known from robot mapping. However, it does not blur the measured information onto the grid cells. The proposed change detection method applies the Dempster-Shafer theory to identify conflicting evidence along the laser pulse propagation path. Additional attributes are considered to decide whether detected changes are of man-made origin or occurring due to seasonal effects. The concept of online change detection has been successfully validated in offline experiments with recorded ALS data streams. Results are shown for an urban test site at which multi-view ALS data were acquired at an interval of one year.

Keywords: Airborne laser scanning, LiDAR, change detection, multi-aspect, multi-temporal data analysis

1. Introduction

1.1. Problem description

Automatic identification of urban structures and the analysis of their changes are important steps to provide a basis for monitoring and planning. Common tasks in this context are the documentation of urban development, surveying of construction sites, or damage inspection after disasters. In particular, the automatic acquisition of buildings and their 3D geometry is of great interest, which is confirmed by the growing number of scientific papers on this topic (Rottensteiner et al., 2013). Data that are analyzed in many of these studies are typically obtained by area-wide acquisition and stereo analysis of high-resolution aerial images (Leberl et al., 2012). Another established technique to deliver 3D data of the terrain is airborne laser scanning (ALS), which is usually carried out with a nadir or near-nadir looking sensor in a strip-wise fashion.

In contrast to nadir imaging or scanning, an oblique forward-looking laser scanner like those used in obstacle warning systems for helicopters (Schulz et al., 2002) can be utilized to create 3D point clouds with full terrain coverage, which is achievable by combining the ALS data from multiple flight paths with varying azimuth angle. This configuration allows the acquisition of facades and rooftops with nearly the same point density (i.e., the same num-

ber of points per unit surface area). However, to be able to use data from multiple ALS scans of the same urban area, a basic requirement is an accurate alignment of the data. On the one hand, this co-registration is necessary to merge multi-view (multi-aspect) ALS data to form a consistent reference data set. On the other hand, a minimization of spatial discrepancies is essential when comparing multi-temporal ALS data for automatic change detection. The overall positioning accuracy, the average point density, and the average discrepancy between the reference and the current ALS data are the delineating factors that limit the minimum size of detectable changes. Therefore, the change detection method must be scalable to the actual system and survey characteristics. In addition, it must take account of occlusions and missing information within the 3D scene.

ALS is well suited to provide 3D measurements which allow direct comparison of geometric features, but additional requirements must be met by the data acquisition and data analysis if the laser scanner is used to support short-term operations, such as the surveillance of urban areas, terrain-referenced navigation, or detection of rapid changes. Examples can be found in assistance systems for helicopter pilots, landing operations in urban terrain, search and rescue missions, emergency services, or disaster management. These applications require methods for

immediate (on-the-fly) processing of range measurements instead of the classical offline treatment of pre-processed ALS data.

1.2. Overview: different stages of ALS data analysis

The intention to use an ALS system for automatic change detection implies that 3D data of the urban area in question have been acquired at an earlier date, so that currently measured ALS data can be compared to these. In this paper, we address change detection mainly in the case that both the reference data and the current 3D data are acquired by ALS. In addition, we require the respective ALS system to allow access to the component’s raw measurements, i.e. the range data, the scanning geometry, and the IMU/GNSS trajectory (see Section 2). As motivated before, we capture the scene with an oblique forward-looking laser scanner.

Overall, we distinguish two different stages of ALS data acquisition and processing (Fig. 1):

- (1.) The creation of the reference database is not time-critical, i.e. the urban area can be scanned on multiple criss-crossing flight paths, and the raw data are processed and optimized offline. This includes the feasibility of correcting GNSS positioning errors by data from ground-based augmentation stations. In (Hebel and Stilla, 2012), we described a method for object-based analysis and automatic registration of such ALS data, together with a method for the automatic boresight calibration of the ALS system. In the course of the data analysis, local principal components are computed at each 3D point, and a region growing technique is used with the aim of ground level segmentation. Within each of the overlapping point clouds, planar shapes are detected by an iterative combination of RANSAC plane fitting and point-specific region growing. This procedure separates typical parts of buildings from clutter objects, such as bushes or trees. To assign identical (homologous) planar shapes across overlapping point clouds, we derive several geometric attributes and evaluate distances of feature vectors. Planarity constraints for these plane-to-plane correspondences are then transferred into systems of linear equations to determine both the boresight parameters and the data alignment. Details of these steps can be found in (Hebel and Stilla, 2012). In this paper, we exploit the segmentation results to support the change detection process.
- (2.) During the mission, all the new ALS measurements are to be (i) categorized, (ii) aligned and (iii) compared to the reference data. These three tasks are intended to be performed in line with the data acquisition, which means that the processing is done continuously on the acquired data stream instead of evaluating the complete point cloud. Regarding task (i), we described a fast segmentation method in (Hebel

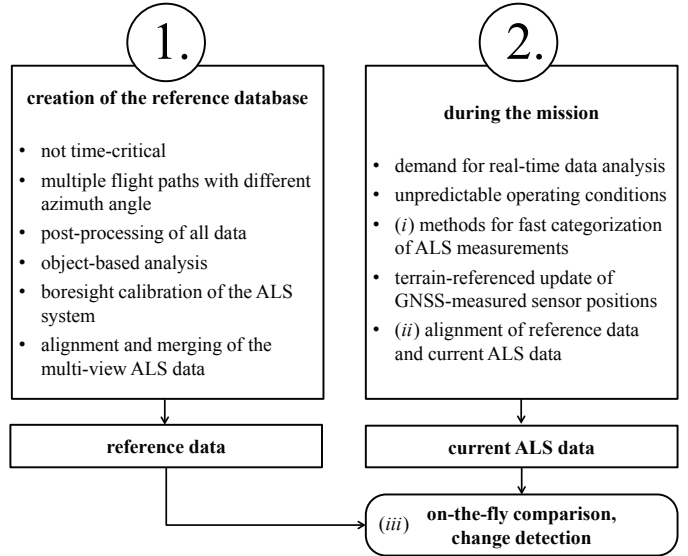


Figure 1: Overview: ALS data acquisition and analysis for automatic change detection.

and Stilla, 2008) that is based on scanline segmentation and grouping of line segments in consecutive scanlines. Matching planar objects, which are identified in both the current data and the reference data, can be used to correct absolute errors of the measured sensor position (Hebel and Stilla, 2010). Even if we have to deal with worse georeferencing accuracy and reliability due to uncorrected GNSS and/or INS drift conditions, this terrain-referenced navigation ensures a permanent alignment of the data, which was defined as task (ii). In this paper, we focus on the comparison task (iii), and we start from the premise that the system calibration and data alignment issues are solved.

Classical methods of change detection in ALS data typically compare the point clouds themselves. In contrast, we include the sensor positions in our considerations. With the assumption of a straight-lined propagation of laser pulses, we state that the space between the laser source and the reflecting 3D point must be empty (or transparent). Additionally, we allow for the occupancy of space behind the reflecting spot to be unknown, as long as it is not affected by other laser measurements. This approach handles occlusions and changes implicitly, such that the latter are identifiable by conflicts of empty space and occupied space along the direction of the laser pulse (which we call henceforth “laser beam”). In robot mapping, such information is often managed in so-called occupancy grids (Moravec and Elfes, 1985). In this paper, we adapt some of these concepts for the use with ALS data. However, instead of evaluating occupancy conflicts on the grid cells themselves, we identify these conflicts at the exact position of the measured 3D points. From a methodical point of view, the presented approach is designed for a future implementation for on-board processing in ALS systems.

This means that the algorithms have been adapted to the boundary conditions described above. With our experimental system and implementation, it was not possible to access or process the data in realtime, but ALS-system manufactures are encouraged to utilize these concepts in their future development.

In the next section, we give an overview of related work on change detection and occupancy grids. Section 2 summarizes the principles of ALS and direct georeferencing. Our methodology is explained in Section 3. A description of our ALS setup and experimental results can be found in Section 4. Finally, Section 5 presents a discussion and our conclusions.

1.3. Related work

In the last twenty years, various academic and industrial research groups have investigated automatic techniques for urban change detection. Most of them approach this task with different intentions and therefore different sensors (Hinz, 2004). Typical examples are the automatic update of building databases and the maintenance/refinement of city models and geographic information systems (GIS). In these examples, the data acquisition can usually be postponed until conditions are optimal (e.g., weather, daytime, season), such that area-wide 3D data can well be obtained by photogrammetric reconstruction from overlapping high-resolution aerial images (Gruber, 2007; Leberl et al., 2012). Synthetic aperture radar (SAR), especially interferometric SAR (InSAR), is also qualified for large-scale urban data acquisition, and it represents a daylight- and weather-independent data source. In a comparison of InSAR and ALS for automatic building reconstruction, Stilla et al. (2003) concluded that building reconstruction is quite possible from InSAR data. Meanwhile, the achievable level of detail can even compete with laser scanning (Schmitt and Stilla, 2011).

Considering the requirements during stage (2.) in Fig. 1, ALS has several additional advantages when compared with the other established techniques for 3D data acquisition and processing. While the InSAR principle requires a side-looking illumination of the scene, an advantage of ALS is the acquisition of 3D data even in the direction of flight. The use of ALS for change detection with regard to buildings has been proposed, for instance, by Murakami et al. (1999). Typically, a digital surface model (DSM) is generated by interpolating the 3D points onto a 2D grid, and changes are detected by computing the difference of these DSM data. To increase the reliability of the change detection results, Vögtle and Steinle (2004) classify the laser points into the classes bare-earth, building, and vegetation. We have described a similar classification approach in (Hebel and Stilla, 2008, 2012) which is used to optimize the automatic registration of overlapping point clouds. The analysis of multi-temporal ALS data is sometimes proposed to assess damage to buildings, e.g., after earthquakes. Hommel (2009) puts strong emphasis on the elimination of vegetation in the ALS data, as this class of

points could be misinterpreted, depending on the foliation state of the vegetation in the different data sets. A similar argumentation given by Rutzinger et al. (2010) was also confirmed in our experiments. However, other applications are conceivable wherein the detection and analysis of urban vegetation are of prime importance. A thorough study on DSM-based change detection methods for urban areas and a detailed survey of related work can be found in (Matikainen et al., 2010).

Unlike the comparison of DSMs, the applications mentioned in Section 1.1 require a different strategy for data processing. There are two reasons for this: (i) we consider oblique views that lead to varying occlusions and point density depending on the aspect angle, (ii) the comparison of current ALS data to given reference data must be executable in line with the data acquisition.

In robotics, similar boundary conditions occur in the simultaneous localization and mapping (SLAM) problem, if ranging sensors are used to generate global maps from local and uncertain sensor data (e.g., sonar, radar, or laser scanning). Most commonly, 2D maps that are horizontal projections of 3D space are taken as a basis. Moravec and Elfes (1985) were the first to represent these maps as 2D arrays of cells labeled *unknown*, *empty*, and *occupied*, with values ranging from 0 to 1 to define the “degree of certainty”. Puente et al. (1991) distinguish two different approaches to fuse information within such occupancy grids. These approaches are: (a) probabilistic estimation based on Bayes’ theorem, and (b) the combination rule of the Dempster-Shafer theory of evidence (Shafer, 1976).

Detailed work on autonomous navigation of mobile robots by a combination of probabilistic occupancy grids with neural networks was done by Thrun (1998). Pellenz and Paulus (2008) describe and compare some examples of robot navigation and 2D map generation found at the “RoboCupRescue” competition. Probabilistic occupancy grids have even been proposed for 3D object recognition (Yapo et al., 2008). Instead of a fixed-size 3D grid, Hornung et al. (2013) use an adaptive octree representation together with a probabilistic occupancy estimation to generate volumetric 3D environment models.

The evidence theory of Dempster-Shafer is commonly used for data fusion (Rottensteiner et al., 2004). In the context of occupancy models, it can substitute the probabilistic approach (Zou et al., 2000; Grabe et al., 2009). There it has the advantage of evaluating conflicting information implicitly, which can be utilized to detect object movements in the scene (Moras et al., 2011). In this paper, we evaluate such conflicts in multi-view and multi-temporal ALS data, which we organize in (but not interpolate to) 3D grids. Similarly, Himmelsbach et al. (2008) proposed to use a 2.5D occupancy grid that acts like a hash table for the retrieval of 3D points in their 3D object perception system. A description of the strengths and weaknesses of a 3D-based approach is given in the next sections.

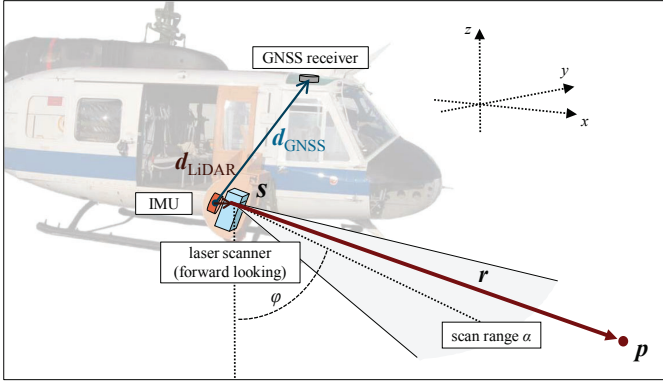


Figure 2: Exemplary ALS sensor carrier and configuration.

2. ALS data acquisition and direct georeferencing

Since an ALS system consists of several spatially separated parts, the mutual placement and alignment of these elements on the aircraft is of great importance when combining the complementary information of all components. While metering the aircraft’s attitude, the lever arms ($\mathbf{d}_{\text{LiDAR}}$, \mathbf{d}_{GNSS}) of laser scanner, GNSS receiver (global navigation satellite system, e.g., GPS, the Global Positioning System) and IMU (inertial measurement unit) are taken into account to transfer the positional coordinates to the laser scanner’s center. Fig. 2 illustrates our configuration, which can be considered as a typical ALS setup, despite the fact that we use an oblique forward-looking laser scanner. A detailed description of our specific ALS system can be found in Section 4, or more thoroughly in (Schatz, 2008).

The laser scanner is the core element of the ALS system. It makes use of the time-of-flight distance measurement principle, e.g. by estimating the range corresponding to the echo pulses as they can be found by constant fraction discrimination or full waveform analysis (Stilla and Jutzi, 2009). Opto-mechanical beam scanning provides a specific scan pattern, in which a distance r_L measured at time t is georeferenced according to scanner geometry as well as position and orientation of the sensor. With the navigational information \mathbf{s} (sensor position) and R_N (sensor orientation) relating to the laser scanner’s center, \mathbf{r}_L is directly georeferenced in the following way:

$$\mathbf{p} = \mathbf{s} + R_N \circ R_B \circ R_S \circ \mathbf{r}_L . \quad (2.1)$$

The above equation is given with the following notations:

\mathbf{s} : 3D position of the laser scanner at time t in a Cartesian geographic coordinate system (e.g., ECEF),

\mathbf{r}_L : distance measured by the laser scanner, given as a Euclidean vector $(0, 0, r_L)^T$,

R_S : 3×3 rotation matrix which describes the scanning geometry,

R_B : 3×3 boresight matrix (relative orientation of IMU and laser scanner),

R_N : 3×3 rotation matrix which describes the orientation of the IMU in 3D space,

\mathbf{p} : coordinates of the resulting “laser point”.

If \mathbf{r} abbreviates the oriented distance vector \mathbf{r}_L , this equation simplifies to

$$\mathbf{p} = \mathbf{s} + \mathbf{r} . \quad (2.2)$$

Direct georeferencing of laser range measurements provides a data acquisition method that is appropriate for airborne surveying. However, the accuracy of the derived 3D point clouds is affected by several influencing factors, reflecting the complexity of the ALS system (Schenk, 2001). We have summarized and quantified these influences in (Hebel and Stilla, 2012), where we also discuss possible improvements to the sensor system and data processing to reduce or avoid these error sources. The overall point positioning accuracy is one of the crucial factors influencing the expectable exactness of the following change detection procedure.

3. Strategy for data processing

Within classical occupancy grids, the data are downsampled or interpolated to match the grid cells. Consequently, the details and the accuracy of detectable changes would be bounded by the resolution of the occupancy grid, while a fine-grained grid would lead to a huge memory consumption.

Instead of evaluating the occupancy of space relating to entire cells of an occupancy grid, we do this for the exact positions of the measured 3D points. The grid structure is only used as a spatial collection of links to the unmodified data, thus providing information on the proximity of laser “beams” and points. In stage (1.), the reference data are assigned to a 3D grid that covers the complete urban area. Fig. 3 illustrates such a 3D grid and the process of ALS data acquisition. During stage (2.), this grid structure allows us to perform fast search operations, so we can evaluate whether current ALS measurements confirm or contradict previous information in the database. Furthermore, the cell size of the grid can be chosen comparatively wide (e.g., five times the average point-to-point distance), resulting in moderate memory requirements. Since the 3D grid is only used as a search structure, the selection of the cell size has only minor impact on the results.

3.1. Generation of the database

In stage (1.), each laser pulse’s origin \mathbf{s} is stored in an indexed list \mathbf{L} , together with the (oriented) measured range \mathbf{r} , such that $\mathbf{p} = \mathbf{s} + \mathbf{r}$ are the coordinates of the respective laser point. The sensor position \mathbf{s} and the orientation R_N are interpolated from the synchronously recorded GNSS/IMU information which is typically captured with a

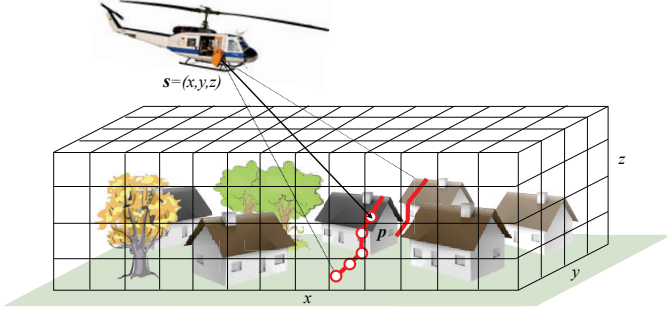


Figure 3: ALS data acquisition and 3D grid.

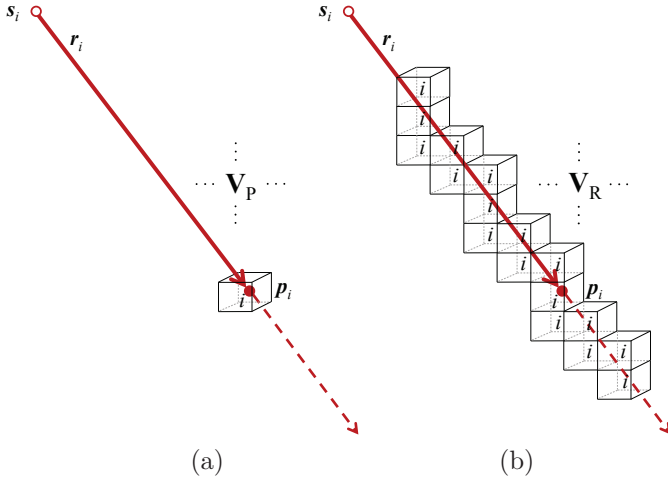


Figure 4: (a) The index i of a point \mathbf{p}_i is stored in the corresponding cell of the 3D grid \mathbf{V}_P . (b) The same index i of the associated “beam” $(\mathbf{s}_i, \mathbf{r}_i)$ is distributed among cells of the 3D grid \mathbf{V}_R .

frequency lower than the pulse repetition rate of the laser scanner. If multiple echoes are received for a single laser pulse, these simply lead to multiple entries in \mathbf{L} . Furthermore, let \mathbf{r}_0 denote the respective unit vector $\mathbf{r}/\|\mathbf{r}\|$. Two 3D grids \mathbf{V}_P and \mathbf{V}_R (Fig. 4) as depicted in Fig. 3 are filled with indices of \mathbf{L} in the following way: Each index $i \in \mathbf{L}$ is included in a single cell of \mathbf{V}_P according to the 3D position of the laser point \mathbf{p}_i that corresponds to this index. Therefore, \mathbf{V}_P simply represents an index-based rasterization of the point cloud. Beyond that, \mathbf{V}_R is used to store all indices of laser beams that traverse the grid cells. To cope with this task, we implemented a 3D variant of Bresenham’s algorithm (Bresenham, 1965), that is well-known in computer graphics for efficient raster line drawing. For a single laser range measurement $(\mathbf{s}_i, \mathbf{r}_i)$, Fig. 4 illustrates how its index i is distributed among cells of \mathbf{V}_P and \mathbf{V}_R . Each cell in \mathbf{V}_P or \mathbf{V}_R can receive either none, one or multiple indices, depending on the number of laser points contained in that cell, or depending on the number of laser beams that run through that cell, respectively.

3.2. Modeling the occupancy of space

Following the terminology of the Dempster-Shafer theory, let U denote the universal set that contains all pos-

sible states of the observed system. In our case, we observe the occupancy of space at a given 3D position, so $U = \{emp, occ\}$ is the universal set, where *emp* and *occ* are abbreviations for “empty” and “occupied”. There is no need to introduce a third label “occluded”, since occlusions are implicitly modeled as unknown space, which is described later on in this section. The power set 2^U of U is given as the set $\{\emptyset, \{emp\}, \{occ\}, U\}$. A so-called belief mass in the interval $[0, 1]$ is assigned to each element of this power set, with the additional properties that the empty set \emptyset has zero mass, and the sum of all other masses is one:

$$m : 2^U \rightarrow [0, 1], \quad m(\emptyset) = 0, \quad \sum_{A \in 2^U} m(A) = 1. \quad (3.1)$$

An assignment that fulfills these criteria is called “basic belief assignment”. The Dempster-Shafer theory makes use of the mass assignment to define upper and lower bounds of an interval that contains the classical probability. These bounds are called “plausibility” and “belief”. Except for equation (3.1), the value of $m(U)$ does not concern $\{emp\}$ or $\{occ\}$ itself, as each of these has its own mass. Instead, the mass $m(U)$ of the universal set U is interpreted as the degree of ignorance. If $m(U)$ equals one, this means that the occupancy of space at the given position is completely unknown. I.e., the Dempster-Shafer theory allows for the explicit representation of ignorance, which means that a lack of information can be distinguished from uncertainty.

From a single laser range measurement $\mathbf{p} = \mathbf{s} + \mathbf{r}$, we get the information that the space in front of \mathbf{p} (seen from \mathbf{s}) is *empty*, and the space at \mathbf{p} itself is *occupied*. Anywhere else, the occupancy of space remains *unknown*. Intuitively, a single laser point is not interpreted as a pinpoint phenomenon. Instead, we associate a spatially extended appearance with it. There are three reasons for this: First, the physical properties of the laser pulse propagation lead to a spatially and temporally extended laser spot (footprint). Second, the position of a measured laser point is somewhat uncertain due to errors in direct georeferencing and misalignment of the data. Third, the size of the smallest observable and discriminable structures depends on the distance between neighboring points, so the spatial extent of a laser point should be modeled in accordance with the average point density (points per unit surface area at ground level). To model a gradual transition between the states *empty* and *occupied* (and *unknown*), we define the impact of a laser range measurement $\mathbf{p} = \mathbf{s} + \mathbf{r}$ on the assignment of masses to an arbitrary position \mathbf{q} in 3D space in the following way:

First, let d_x denote the longitudinal distance of \mathbf{q} to \mathbf{p} (see Fig. 5):

$$d_x = (\mathbf{q} - \mathbf{p}) \cdot \mathbf{r}_0. \quad (3.2)$$

Similarly, let d_y denote the transverse distance of \mathbf{q} to \mathbf{p} :

$$d_y = \|(\mathbf{q} - \mathbf{p}) \times \mathbf{r}_0\|. \quad (3.3)$$

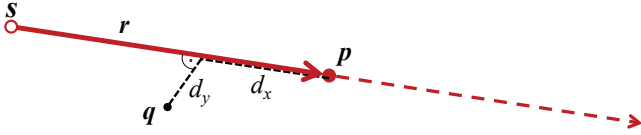


Figure 5: Longitudinal and transverse distances of q to p .

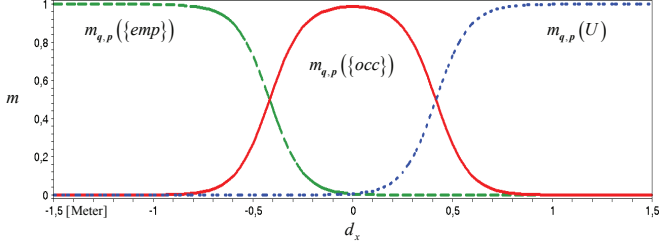


Figure 6: Belief assignment to points on the laser beam ($d_y = 0$).

On the basis of the distances d_x and d_y , we define the following belief masses (at position q caused by p):

$$\begin{aligned}
 m_{q,p}(\emptyset) &= 0, \\
 m_{q,p}(\{emp\}) &= \left(1 - \frac{1}{1 + e^{-\lambda d_x - c}}\right) \cdot e^{-\kappa d_y^2}, \\
 m_{q,p}(\{occ\}) &= \left(\frac{1}{1 + e^{-\lambda d_x - c}} - \frac{1}{1 + e^{-\lambda d_x + c}}\right) \cdot e^{-\kappa d_y^2}, \\
 m_{q,p}(U) &= 1 - m_{q,p}(\{emp\}) - m_{q,p}(\{occ\}).
 \end{aligned} \quad (3.4)$$

By definition, (3.4) fulfills the conditions (3.1), so these equations represent a basic belief assignment. The respective first factor in $m_{q,p}(\{emp\})$ and $m_{q,p}(\{occ\})$ is composed of sigmoid functions. One of these is used to describe free space in front of p , the other characterizes the lack of knowledge behind the laser point. In between, the inverse sum of the sigmoid functions reflects the actual occupancy at the position of p . The longitudinal extent of occupied space at p is controlled by the parameter c , and the gradual transition from *empty* to *occupied* to *unknown* is controlled by λ . Fig. 6 shows this interaction of the sigmoid functions, with the parameters in equations (3.4) set to $\lambda=12$ and $c=5$. Outside of the beam axis, the second factor in $m_{q,p}(\{emp\})$ and $m_{q,p}(\{occ\})$ describes a Gaussian profile that is controlled by the parameter κ and fades to ignorance (transverse extent of the laser point/beam). Fig. 7 shows exemplary graphs of the nonzero belief masses around p .

The parameters (λ, c, κ) describe the fuzziness of the laser points. As mentioned above, they should be chosen to conform to the physical characteristics of the laser range measurements in the survey. This means that $m_{q,p}(\{occ\})$ should reflect the point positioning accuracy, which is influenced, for example, by the range resolution of the specific laser scanning device. But it is just as important that $m_{q,p}(\{occ\})$ conforms to the average point-to-point distance in the scene: if $m_{q,p}(\{occ\})$ is too narrow, most range measurements would not interfere with another in

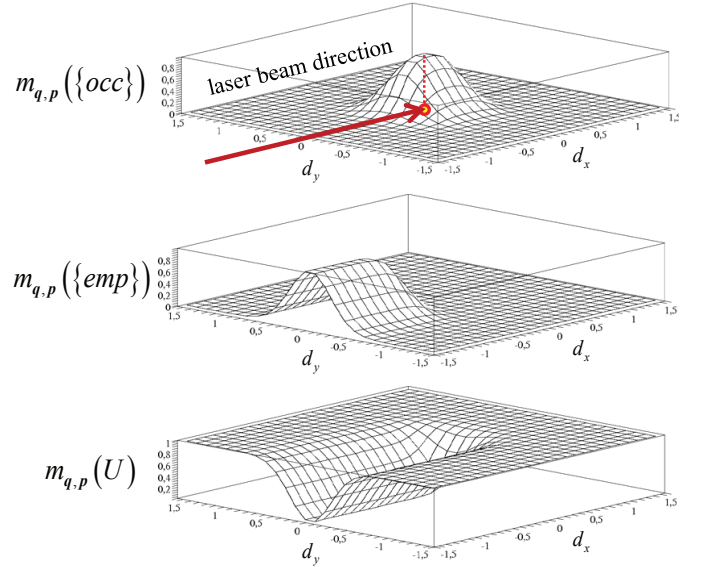


Figure 7: Comparison of belief masses near p (*occupied*, *empty*, *unknown*), $\lambda=12$, $c=5$, $\kappa=8$.

the following change detection approach. Otherwise, if $m_{q,p}(\{occ\})$ is too broad, this would lead to false detections and degraded accuracy. As a rule of thumb, κ should be chosen such that the FWHM (full width at half maximum) of $e^{-\kappa d_y^2}$ amounts to twice the average point-to-point distance within a single strip, thus leading to an area-filling overlap of neighboring “points”. However, if the point positioning accuracy and data alignment are even worse than this distance, κ has to be decreased to take account of this. The setting of the parameters (λ, c) should follow that of κ , such that $m_{q,p}(\{occ\})$ puts on nearly circular shape (see top of Fig. 7). An additional discussion on the setting and the influence of these parameters can be found in Section 5.

3.3. Combination of evidence from different measurements

In the previous section we considered a single range measurement $p = s + r$ and its influence on the mass assignment to a position q . In case we observe two or more laser beams in the neighborhood of q , we need to combine the respective mass assignments. Let $p_1 = s_1 + r_1$ and $p_2 = s_2 + r_2$ be two independent laser range measurements. Equations (3.4) define different sets of mass assignments to the position of q , which are given by m_{q,p_1} and m_{q,p_2} , respectively. For better readability, we abbreviate $m_{q,p_1}(\{emp\})$ to $m_1(e)$ and $m_{q,p_1}(\{occ\})$ to $m_1(o)$ etc.

Using these notations, we apply Dempster’s rule of combination (Dempster, 1967) to calculate the joint mass m from the sets m_1 and m_2 . The amount C of conflict between the two mass sets is measured as follows (“empty in m_1 and occupied in m_2 , or vice versa”):

$$C = m_1(e) m_2(o) + m_1(o) m_2(e). \quad (3.5)$$

Within Dempster's rule of combination, conflicting evidence is ignored, which is achieved by the normalization factor $(1 - C)$ as follows:

$$\begin{aligned} m(e) &= \frac{m_1(e)m_2(e) + m_1(e)m_2(U) + m_1(U)m_2(e)}{1 - C}, \\ m(o) &= \frac{m_1(o)m_2(o) + m_1(o)m_2(U) + m_1(U)m_2(o)}{1 - C}, \\ m(U) &= \frac{m_1(U) \cdot m_2(U)}{1 - C}, \quad m(\emptyset) = 0. \end{aligned} \quad (3.6)$$

The operations (3.6) are commonly written as $m = m_1 \oplus m_2$ and result in a new set m of belief masses that is a combination of m_1 and m_2 . It should be noted that \oplus is commutative and associative. Therefore, even an arbitrary number of belief assignments can be combined by \oplus in a unique way.

3.4. Change detection

In stage (2.), we decide whether a new ALS measurement $\mathbf{q} = \mathbf{s}_Q + \mathbf{r}_Q$ confirms or contradicts the mass assignments which we obtain from old measurements that we recorded in \mathbf{L} . Conflicts occur if the laser beam $(\mathbf{s}_Q, \mathbf{r}_Q)$ traverses *occupied* space in front of \mathbf{q} , or if \mathbf{q} comes to lie in a region that is marked *empty*.

We address the latter case first (conflict type A, Fig. 8a). Let $v_q \subset \mathbf{V}_R$ denote the cells of \mathbf{V}_R which correspond to the position of \mathbf{q} . This subset v_q may comprise only one cell or an additional neighborhood. It is expected that v_q contains the indices of laser beams in \mathbf{L} which affect the mass assignment to the position of \mathbf{q} . In Fig. 8a, these laser beams are depicted with thin and partly dotted lines in blue color. Let I_q be the set of indices which are associated with v_q . On the one hand, we consider the joint mass $m_q^{\textcircled{1}}$ resulting from all old measurements \mathbf{p}_i in \mathbf{L} where $i \in I_q$:

$$m_q^{\textcircled{1}} = \bigoplus_{i \in I_q} m_{\mathbf{q}, \mathbf{p}_i}. \quad (3.7)$$

On the other hand, the mass assignment $m_q^{\textcircled{2}}$ that we obtain from the (single) new measurement $\mathbf{q} = \mathbf{s}_Q + \mathbf{r}_Q$ itself is given as:

$$m_q^{\textcircled{2}}(\{emp\}) = m_q^{\textcircled{2}}(U) = 0, \quad m_q^{\textcircled{2}}(\{occ\}) = 1. \quad (3.8)$$

Based on these assignments, we can identify conflicts between $m_q^{\textcircled{1}}$ and $m_q^{\textcircled{2}}$ in the same way as it is done in equation (3.5), resulting in a measure of conflict $C_q = m_q^{\textcircled{1}}(\{emp\})$.

The other type of conflict is caused by occupied space that is encountered while the laser pulse propagates from \mathbf{s}_Q to \mathbf{q} (conflict type B, Fig. 8b). To find these conflicts, we extend the list \mathbf{L} to include mass assignments to every point \mathbf{p} in \mathbf{L} . We initialize these masses to an *unknown* occupancy:

$$m_{\mathbf{p}}^{\textcircled{2}}(\{emp\}) = m_{\mathbf{p}}^{\textcircled{2}}(\{occ\}) = 0, \quad m_{\mathbf{p}}^{\textcircled{2}}(U) = 1. \quad (3.9)$$

We use Bresenham's line drawing algorithm in 3D to identify grid cells in \mathbf{V}_P through which the laser beam $(\mathbf{s}_Q, \mathbf{r}_Q)$

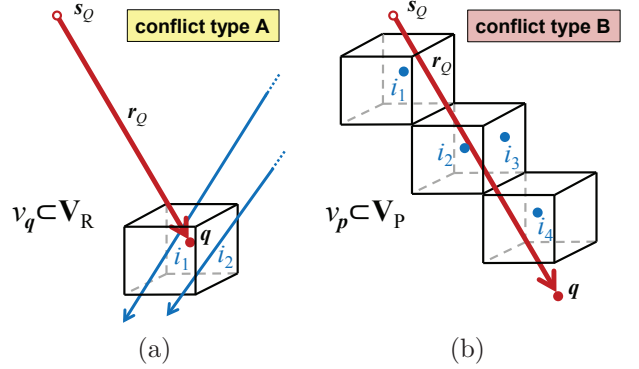


Figure 8: Conflicts between reference data (blue) and the current measurement $\mathbf{q} = \mathbf{s}_Q + \mathbf{r}_Q$ (red, bold): (a) *empty* space at \mathbf{q} , (b) *occupied* space along \mathbf{r}_Q .

passes. Let v_p denote this subset of \mathbf{V}_P , and let I_p be the set of indices associated with v_p . These indices reveal the laser points in \mathbf{L} (blue points in Fig. 8b) that are affected by the current laser beam $(\mathbf{s}_Q, \mathbf{r}_Q)$. For every position \mathbf{p}_i with $i \in I_p$, we update the mass set $m_{\mathbf{p}_i}^{\textcircled{2}}$ to the joint mass of $m_{\mathbf{p}_i}^{\textcircled{2}}$ and $m_{\mathbf{p}_i, \mathbf{q}}$:

$$m_{\mathbf{p}_i}^{\textcircled{2}} \leftarrow m_{\mathbf{p}_i}^{\textcircled{2}} \oplus m_{\mathbf{p}_i, \mathbf{q}} \quad \forall i \in I_p. \quad (3.10)$$

After the current laser scanning process has left the reach of a point \mathbf{p} in the database, we evaluate the accumulated mass assignment $m_{\mathbf{p}}^{\textcircled{2}}$ and its conflict to $m_{\mathbf{p}}^{\textcircled{1}}$, which is given analogous to equation (3.8). We obtain $C_p = m_{\mathbf{p}}^{\textcircled{2}}(\{emp\})$ as a measure of conflict.

3.5. Including additional attributes

The steps described in the previous Sections 3.1 to 3.4 fit well into the boundary conditions that are set by the multi-view ALS data acquisition and the applications described in Section 1.1. As required, the comparison of multi-temporal ALS data can be accomplished during the data acquisition, since each new range measurement is tested separately for possible conflicts with the reference data (i.e. without the need to address the entire point cloud). Furthermore, occlusions are handled implicitly.

Up to this point, segmentation and classification results did not find their way into the change detection procedure. However, these results are available, as they arise from the generation of the reference data (Hebel and Stilla, 2012) and the scan-line analysis of current ALS measurements (Hebel and Stilla, 2008). In the following, we use this additional information to improve the detection performance and the automatic interpretation of detected changes. Dependent on the respective object class, we control the impact of range measurements $(\mathbf{s}, \mathbf{r}) \in \mathbf{L}$ on the mass assignments in 3D space.

One drawback of the approach presented so far is the missing distinction of continuous surfaces and clutter (e.g., vegetation). The problem herein lies in the ability of laser pulses to partially penetrate vegetation, which is caused by the spatial extent of the laser spots (Reitberger et al.,

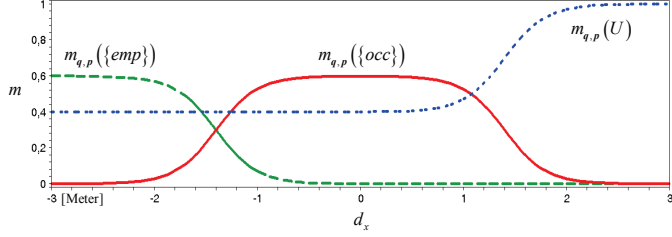


Figure 9: Belief assignment to points on the laser beam ($d_y = 0$), in case this measurement is associated with vegetation.

2009). This characteristic is not yet included in the model described by equations (3.4). As a consequence, a single laser pulse can lead to positions in its propagation path that are marked *occupied* by one echo but *empty* by subsequent echoes. These self-induced conflicts of mass assignments occur because multiple echoes are treated independently in \mathbf{L} , but in fact these measurements are correlative. However, even independent measurements (\mathbf{s}, \mathbf{r}) that are associated with (unchanged) vegetation can result in conflicts, as these 3D positions are subject to considerable statistical fluctuations. For these reasons, it is proposed to model vegetation with parameters different from those of continuous surfaces. A possible way to represent the fuzziness of vegetation is to increase the degree of ignorance $m(U)$ and the dimensions of *occupied* space. This is achieved by modifications of (3.4) with weighting factors f_e and f_o and alternative parameters ($\hat{\lambda}, \hat{c}, \hat{\kappa}$) in the following way:

$$\begin{aligned} m_{\mathbf{q},\mathbf{p}}(\{\text{emp}\}) &= f_e \cdot \left(1 - \frac{1}{1 + e^{-\hat{\lambda}d_x - \hat{c}}}\right) \cdot e^{-\hat{\kappa}d_y^2} , \\ m_{\mathbf{q},\mathbf{p}}(\{\text{occ}\}) &= \frac{f_o \cdot e^{-\hat{\kappa}d_y^2}}{1 + e^{-\hat{\lambda}d_x - \hat{c}}} - \frac{f_o \cdot e^{-\hat{\kappa}d_y^2}}{1 + e^{-\hat{\lambda}d_x + \hat{c}}} , \\ m_{\mathbf{q},\mathbf{p}}(U) &= 1 - m_{\mathbf{q},\mathbf{p}}(\{\text{emp}\}) - m_{\mathbf{q},\mathbf{p}}(\{\text{occ}\}) . \end{aligned} \quad (3.11)$$

According to these equations and analogous to Fig. 6, Fig. 9 shows the mass assignment to positions along the laser beam. Same as λ , c and κ in equations (3.4), reasonable values for the parameters depend on the survey and system characteristics. In this example, $f_e = 0.6$ and $f_o = 0.6$ are the weighting factors that are used to ensure a uniformly high degree of ignorance and low occupancy. Likewise, $\hat{\lambda} = 5$, $\hat{c} = 7$ (and $\hat{\kappa} = 2$) are the parameters which model a higher fuzziness of the laser point (approximately two to three times higher if compared with the standard setting). This setting is used to describe the occupancy of space for all measurements that have been assigned to the vegetation class. Different ways are available to perform this classification automatically:

- If several echoes are detected for one emitted laser pulse, all but the last echo can be ascribed to vegetation.
- In case a full waveform laser scanner is employed, veg-

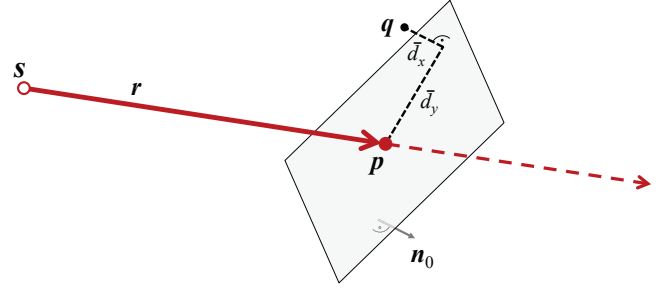


Figure 10: Distances of \mathbf{q} to the local plane at \mathbf{p} .

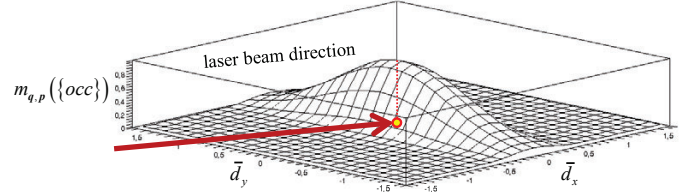


Figure 11: Belief mass of the state *occupied* near \mathbf{p} , in case \mathbf{p} is embedded into a continuous surface.

etation can be detected by a detailed analysis of the echo's waveform (Reitberger et al., 2009).

- The segmentation method described in (Hebel and Stilla, 2012) provides an evaluation of the local geometry by principal component analysis (PCA). In particular, the method identifies 3D points that are embedded into continuous surfaces (e.g., ground level, parts of buildings) and separates these from irregular points. The latter are assigned to the vegetation class.

In the extended model, range measurements (\mathbf{s}, \mathbf{r}) $\in \mathbf{L}$ fulfilling one or more of the above criteria affect the assignment of belief masses to positions in 3D space under equations (3.11) instead of (3.4).

An obvious way to refine the model is to account for the orientation of continuous surfaces. If local PCA clearly reveals a local normal direction, the distribution of $m_{\mathbf{q},\mathbf{p}}(\{\text{occ}\})$ should be spread out along the detected surface. Let $\mathbf{p} = \mathbf{s} + \mathbf{r}$ denote such a range measurement listed in \mathbf{L} , and let \mathbf{n}_0 denote the corresponding unit normal vector that is found by local PCA as the eigenvector to the smallest eigenvalue. To avoid ambiguity, \mathbf{n}_0 is oriented to the same half space as \mathbf{r} , such that $\mathbf{n}_0 \cdot \mathbf{r} \geq 0$ (see Fig. 10). In exchange for d_x and d_y , we define the distances \bar{d}_x and \bar{d}_y in the following way:

$$\begin{aligned} \bar{d}_x &= (\mathbf{q} - \mathbf{p}) \cdot \mathbf{n}_0 , \\ \bar{d}_y &= \|(\mathbf{q} - \mathbf{p}) \times \mathbf{n}_0\| . \end{aligned} \quad (3.12)$$

In the extended model, the impact of $\mathbf{p} = \mathbf{s} + \mathbf{r}$ on the assignment of belief masses to \mathbf{q} at first depends on the Euclidean distance $d = \|\mathbf{q} - \mathbf{p}\|$. If \mathbf{q} is far apart from \mathbf{p} (e.g., $d \geq 3$ m), $m_{\mathbf{q},\mathbf{p}}$ is defined with (d_x, d_y) and (λ, c, κ) according to equations (3.4). Otherwise, if \mathbf{q} lies near to

\mathbf{p} , the same equations are evaluated with the distances (\bar{d}_x, \bar{d}_y) and the parameters ($\lambda, c, \bar{\kappa}$). The parameter $\bar{\kappa}$ is significantly smaller than κ and models a broad distribution of *occupied* space along the estimated surface at \mathbf{p} . Fig. 11 illustrates this distribution for a typical setting $\bar{\kappa} = 1$ (and $\lambda = 12, c = 5$).

4. Experiments and results

The data that we analyzed for this study were acquired during field campaigns in 2008 and 2009, using a RIEGL LMS-Q560 laser scanner (version 2006) in combination with an Applanix POS AV 410 inertial navigation system. All sensors were attached to a helicopter of type Bell UH-1D (Fig. 2). This experimental setup lacks online data access, so we had to simulate the on-the-fly data analysis: All experiments described in this section were conducted in a post-processing mode based on the stream of recorded raw data. With our configuration and settings, each scan line of the laser scanner covered a field of view of 60° subdivided into 1000 angular steps. The inclination angle of the laser scanner was set to 45° while flying with the helicopter’s nose pitched down (Fig. 2 and Fig. 3). Due to aviation security reasons, the minimum flight level had to be restricted to 1000 ft. These boundary conditions led to laser strips with a width of 500 m and an average point-to-point distance of 0.5 m. The table in Fig. 12 lists all urban test sites where data have been acquired, together with the point positioning accuracy that we achieved using the calibration and data alignment methods described in (Hebel and Stilla, 2012).

The experiments concerning change detection were conducted with the “Abenberg” data. In April 2008, ALS data have been acquired at this test site in a cross pattern (Fig. 13a), resulting in an accumulated point cloud which includes 5,400,000 points with an average point density of 16 pts/m². Fig. 14a shows a rendered visualization of these reference data, where each point is gray-value coded according to the echo amplitude, which is derived from full waveform analysis. As described in Section 3.5, we used local PCA and region growing in order to segment and classify the reference data in \mathbf{L} to the classes *ground*, *vegetation*, and *building* (see Fig. 14b). The cell size of \mathbf{V}_R and \mathbf{V}_P was chosen to be $2 \times 2 \times 2$ m³, resulting in two 3D grids of the dimensions $300 \times 300 \times 50$ (which corresponds to $600 \times 600 \times 100$ m³) to cover the area in question. After the distribution of \mathbf{L} -indices among these cells, the memory requirements of \mathbf{V}_P and \mathbf{V}_R amount to 1.1 GB in total. The test site “Abenberg” was scanned again in August 2009, using the same sensors and a similar setting (Fig. 13b).

Based on the recorded data stream of single strips (e.g., number 1 in Fig. 13b), we successively applied the methods described in Section 3. The parameters (λ, c, κ) in equations (3.4) were set to $\lambda=12, c=5, \kappa=8$ as shown in Fig. 6. First results of this experiment are depicted in Fig. 14c. Conflicts of type B with $C_p \geq th$, (threshold $th = 0.5$), are shown in red (objects that have disappeared), whereas

test site	coordinates WGS84	date mm/dd/yy	aspects	points (overlap)	density [pts/m ²]	accuracy [cm]
Munich (TUM)	N 48° 8.94', E 11° 34.04'	09/02/09	4	4,400,000	5.2	10-30
Rendsburg	N 54° 17.94', E 9° 41.28'	04/22/08	5	5,400,000	18.6	10-30
Ruschberg	N 49° 37.18', E 7° 17.33'	09/01/09	3	4,200,000	17.7	5-15
Abenberg	N 49° 14.50', E 10° 57.80'	04/18/08	4	5,400,000	16.1	5-10
		08/31/09	4	6,200,000	21.1	5-10
Kiel	N 54° 19.41', E 10° 8.38'	04/23/08	6	6,600,000	9.9	10-70
Ettlingen (IOSB)	N 48° 56.83', E 8° 24.65'	09/01/09	3	5,000,000	20.0	10-30

Figure 12: Details of the urban test sites, the respective data sets and the achieved point positioning accuracy.

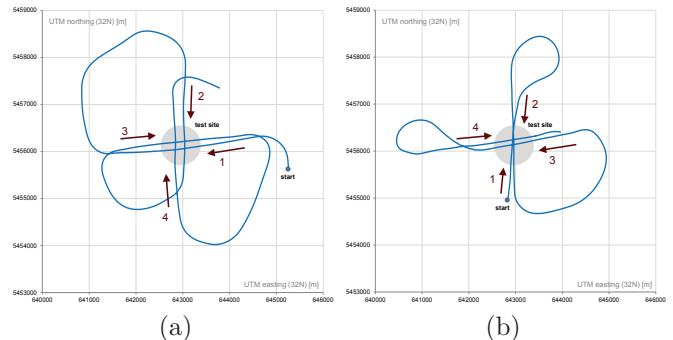


Figure 13: Top view of the helicopter’s trajectory at the test site “Abenberg”: (a) April 18, 2008, (b) August 31, 2009.

conflicts of type A with $C_q \geq th$ are colored yellow (objects that have appeared). In this example, vegetation obviously causes a lot of type A conflicts, which can be ascribed to seasonal influences (April vs. August).

The classification of the reference data (Fig. 14b) allows us to control the influence of data points in the vegetation class ($\hat{\lambda} = 5, \hat{c} = 7, \hat{\kappa} = 2$). Furthermore, we account for the orientation of continuous surfaces ($\bar{d}_x, \bar{d}_y, \bar{\kappa} = 1$). To avoid disturbances by single point clutter, we accept detections only if they occur at least twice within the scan line. The result is shown in Fig. 14d. In addition to the previous color-coding, green points now indicate that these are (most likely) part of an unchanged building ($C_q \leq th$).

The remaining conflicts are mainly caused by moved cars, demolition, and newly constructed buildings. Some details of the results are depicted in Fig. 15. The left column of this figure shows detailed views that have been generated from the 2008 reference data. In direct comparison, the center column shows the respective views of the 2009 data. On the right, the results of automatic change detection are depicted with a manual interpretation and annotation. The “Abenberg Castle” can be seen in the top row (Fig. 15a). Apparently, the cars disappeared from the inner courtyard of the castle, and the construction in front of the castle was finished in between 2008 and 2009. Even the waving flag on the tower resulted in a detection. Fig. 15b shows the most obvious detection, which is the demolition of several houses in the center of Abenberg. Instead of the buildings, only a single car can be found here in 2009. Besides the obvious detections, Fig. 15c shows one of the main advantages of the presented approach: Al-

Abenberg
 N 49° 14.543', E 010° 57.690'
 RIEGL LMS-Q560, Applanix POS AV 410
 point positioning accuracy: ~ 10 cm
 April 18, 2008

Abenberg
 N 49° 14.543', E 010° 57.690'
 RIEGL LMS-Q560, Applanix POS AV 410
 point positioning accuracy: ~ 10 cm
 August 31, 2009

■ conflict type A (appeared)
■ conflict type B (disappeared)
■ verified planar region
■ verified ground level
■ unchanged or previously unknown

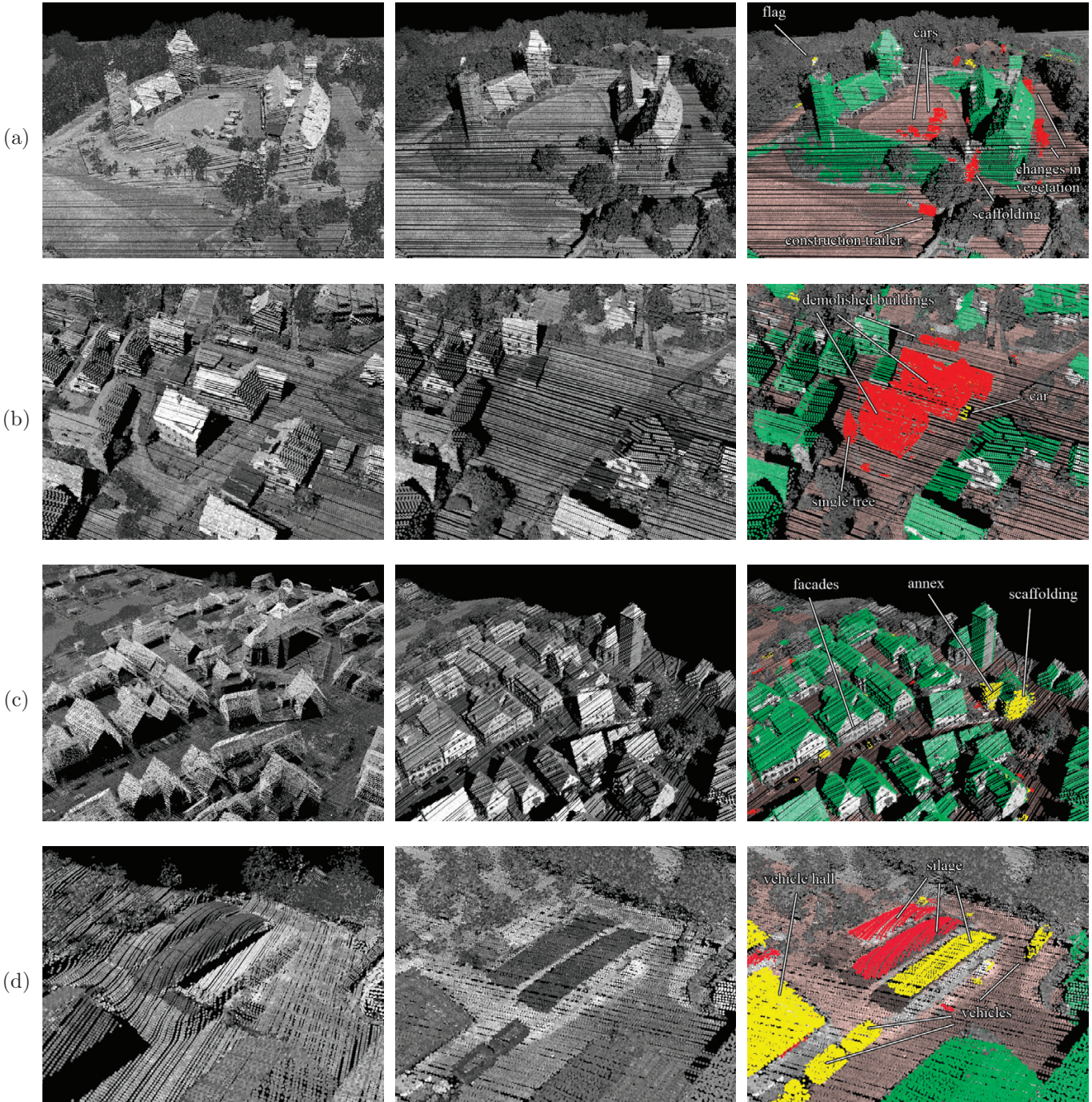
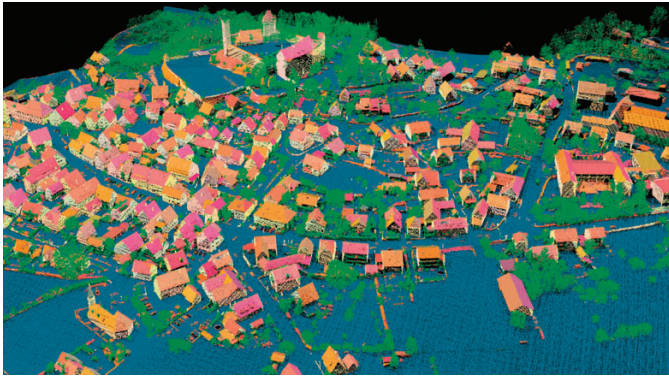


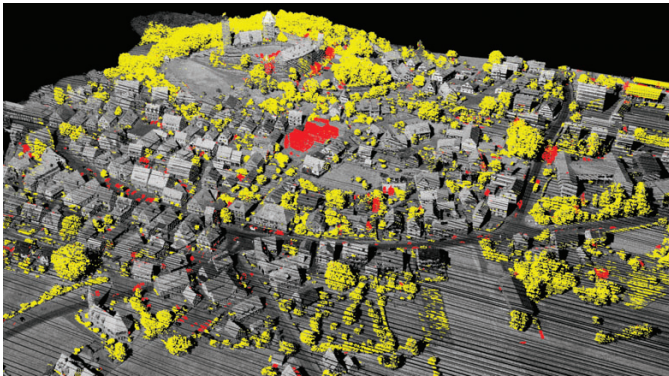
Figure 15: Details of the results: e.g., (a) cars that have disappeared from the inner courtyard of the castle, (b) demolition of several buildings, (c) scaffolded house, (d) farm with new vehicle hall and silage.



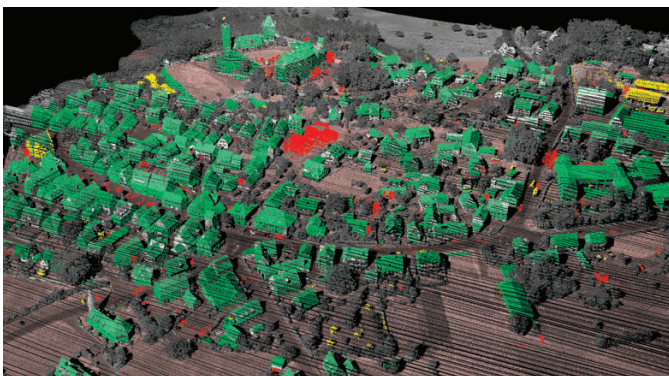
(a)



(b)



(c)



(d)

Figure 14: (a) View of the reference data, (April 2008), (b) classification and segmentation of the reference data, (c) conflicts of mass assignments (August 2009), (d) result of change detection.

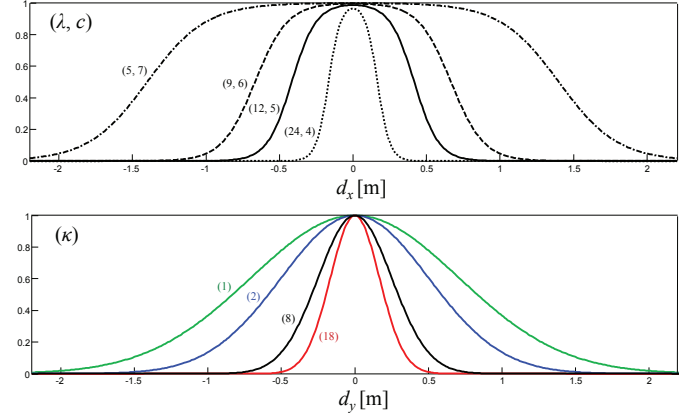


Figure 16: Model of the longitudinal (top) and transverse (bottom) extent of *occupied* space at a laser point p for different settings of λ , c and κ .

though some facades were not present in the reference data (2008) due to incomplete terrain coverage, these structures do not result in a false detection of changes in 2009. Instead, missing reference data are automatically complemented by new measurements. Finally, Fig. 15d depicts a farm with some reconstruction work done in between 2008 and 2009 (vehicle hall), and with some vehicles that have appeared at this place. Changes were also detected at the silage due to different filling levels.

A possible way to evaluate the proposed methods in detail would be to simulate the ALS data acquisition, e.g. with some kind of ray-tracing approach and a synthetic scene. However, it is questionable whether a simulation can reproduce data that is comparable to that of a real ALS system. For a quantitative evaluation with the available real data, we would need the ground-truth of all changes between 2008 and 2009, which we do not have. Nevertheless, we used data of the buildings that can be seen in Fig. 15b. It is out of question which buildings in this part of the scene have changed due to demolition. Together with the segmentation results, it is possible to identify all laser range measurements in the data that correspond to parts of unchanged buildings or to parts of the demolished buildings. This portion of the data yields many examples for conflicts of type B (objects that have disappeared). To get examples for conflicts of type A (objects that have appeared) within the same data, we simply changed the direction of time: the data “Abenberg 2009” were treated as reference data, while the data stream of a single strip from “Abenberg 2008” was investigated for the detection of changes. With this experiment, we were able to analyze which points of unchanged or changed parts of buildings were correctly or incorrectly categorized, depending on different settings of the parameters λ , c and κ and different thresholds th . We used each of the settings $(\lambda, c) \in \{(5, 7), (9, 6), (12, 5), (24, 4)\}$ and $\kappa \in \{1, 2, 8, 18\}$ to model the longitudinal and transverse extent of *occupied* space at the laser points (Fig. 16). For all sixteen combinations of these settings, the measures of conflict

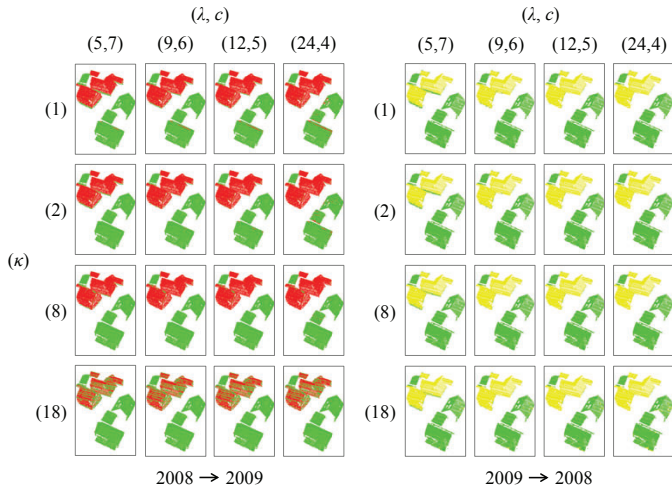


Figure 17: Details of the results obtained with different parameter settings. Left: type B conflicts 2008 \rightarrow 2009, right: type A conflicts 2009 \rightarrow 2008.

C_p (conflicts of type B) were computed with respect to the timeline 2008 \rightarrow 2009. The measures C_q (conflicts of type A) were computed for the timeline 2009 \rightarrow 2008, respectively. The results of this experiment are depicted in Fig. 17, with the previous color-coding and the threshold th set to $th = 0.5$.

In addition to different settings of λ , c and κ , we have set the threshold th to different values in the interval $[0, 1]$, for which we evaluated the rate of detections among measurements on building parts that have changed, and (false) detections on building parts that were unchanged. The first rate corresponds to the probability of detection, while the second is the false alarm rate. In literature, the plot of these rates at different parameter settings is called *receiver operating characteristic*, or *ROC curve*. ROC curves for this experiment are depicted in Fig. 18. Each line in this plot corresponds to a specific setting of (λ, c) and κ as described above, for which the threshold th runs through the interval $[0, 1]$. The “optimal” setting among these examples (if optimality means getting closest to 100% detections and 0% false alarms) was found to be $(\lambda, c, \kappa) = (12, 5, 8)$ with the threshold set to $th = 0.17$, giving a probability of detection of 99% at 1% false alarm rate in this example.

5. Discussion and conclusions

The experiments described in Section 4 demonstrated that spatial changes can be reliably detected, provided that the data are properly aligned. Seasonal changes in vegetation, changes of buildings (e.g., extensions, demolition), and moved cars are found by our automatic method. The minimum size of detectable changes is limited by the point density and the respective point positioning accuracy, which need to be modeled correctly by means of the parameters, i.e. (λ, c, κ) . We evaluated different settings of these parameters to detect changes of buildings (Fig. 17). The ROC curves in Fig. 18 show that reasonable settings

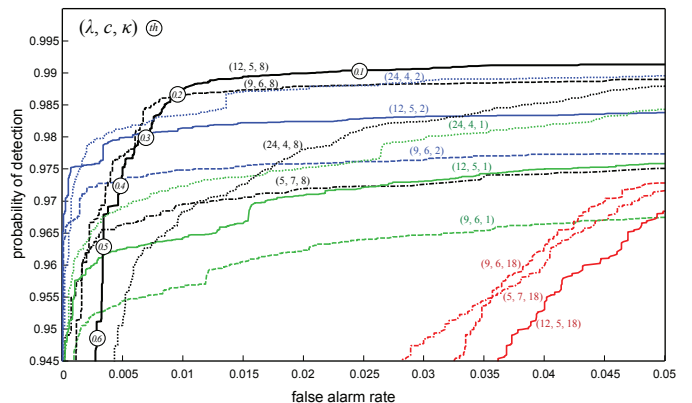


Figure 18: ROC curves showing the probability of detection and false alarm rate for different settings of (λ, c, κ) and different thresholds th (line style and color accord with Fig. 16).

of (λ, c, κ) result in a nearly equally good probability of detection that is greater than 96% for single points, with a false alarm rate below 2%. A reasonable setting of the parameters represents a compromise between the achievable level of detail and the tolerance against data misalignment. As to be expected, a small point density and/or discrepancies between the different data sets result in a low level of detail. If the discrepancies are small, we recommend to set the parameters such that the FWHM of $m_{q,p}(\{occ\})$ amounts to approximately twice the average point-to-point distance within a single strip, so that measurements from different strips will have a significant overlap. In case of large discrepancies, the occupancy of space at the position of p needs to be modeled even broader in order to smooth the registration errors. Anyway, depending on the object class (e.g., vegetation), smoothing of smaller changes without detecting them might be the desired behavior.

Overall, we were able to detect changes of approximately one cubic meter. However, this result is specific to our experimental system and specific to the underlying circumstances during our field campaigns (e.g., point density at ground level). The presented methodology is independent of hardware and survey characteristics, and it can easily be adapted to any airborne or terrestrial laser scanning system.

In this paper, we have presented a framework for ALS-based change detection in urban areas. Our methodology is inspired by (but different from) the concept of occupancy grids, and we implemented Dempster’s rule of combination to fuse multiple measurements. During this process, conflicts between different belief assignments are evaluated with regard to change detection. The main conceptual advantage of the proposed methods is the handling of occlusions as unknown space, which would otherwise require a more complex case-by-case analysis. In contrast to probabilistic approaches, the Dempster-Shafer theory allows an explicit representation of ignorance. Therefore, even partially non-overlapping ALS data can be combined and compared without causing erroneously detections of

changes. Different from the well-known concept of occupancy grids, we evaluate the occupancy of space at the exact 3D positions of the laser points, without declining the given resolution of the laser scanner.

The examples presented in this paper were obtained with an experimental sensor system, for which the data analysis was done offline in order to show the feasibility of the approach. Nevertheless, the proposed methods are inherently realtime capable, as opposed to classical methods of point cloud analysis that start after the complete data set was obtained. The following tasks have to be solved to implement the on-the-fly change detection in practice:

- To generate the reference data in stage (1.), the ALS system (i.e., the laser scanner and the navigational sensors) must allow the recording of all raw data (trajectory data, laser range measurements).
- To perform the online data analysis, the ALS system has to gain realtime access to these raw data during the data acquisition in stage (2.).
- The alignment of the data is crucial to the accuracy of the change detection results. Therefore, the navigational sensor system should preferably be operated in realtime kinematic positioning mode (RTK), which requires a data connection to one or more nearby GNSS reference stations. As an alternative, we proposed the use of the existing 3D data for terrain-referenced navigation (Hebel and Stilla, 2010).
- Search operations within the reference data (points and beams) must be performed very fast. While 3D points can be efficiently organized in an octree or k -d tree, to the best of our knowledge, no such search structure exists for the organization of skew 3D lines. We use the 3D grids \mathbf{V}_P and \mathbf{V}_R instead, in which we store links to the reference data. Depending on the number of data points and the cell size, the memory requirements of \mathbf{V}_R can be quite high (several GB), which has to be taken into account in the hardware design.
- The numerical evaluation of exponential functions in equations 3.4 is rather inefficient, but these calculations can be replaced by look-up tables. Furthermore, the presented techniques have high potential for parallelization, which should be exploited to speed up the data processing.

Modern ALS instruments show a trend toward increasing performance and realtime processing. A typical example is online waveform analysis (e.g., RIEGL VQ-580). For the future, we expect that an efficient implementation of the proposed methods can work in realtime on an operational system, and we expect that the parameters (λ, c, κ) can automatically be set during the data acquisition.

It is possible to perform further semantic analysis of the multi-view ALS data, which can give new impulses to the

interpretation of detected changes. For instance, changes to vehicles in the urban scene can be detected together with an estimation of their motion (Yao et al., 2011). A semantic interpretation of building facades was shown by Tuttas and Stilla (2012), using multi-view ALS data of the test site “Munich (TUM)” which have been acquired with the same ALS system.

References

- Bresenham, J., 1965. Algorithm for computer control of a digital plotter. *IBM Systems Journal* 4, 25–30.
- Dempster, A., 1967. Upper and lower probabilities induced by a multivalued mapping. *Annals of Mathematical Statistics* 38, 325–339.
- Grabe, B., Ike, T., Hoetter, M., 2009. Evaluation method of grid based representation from sensor data, in: *Proceedings of the IEEE Intelligent Vehicles Symposium*, pp. 1245–1250.
- Gruber, M., 2007. UltraCamX, the new digital aerial camera system by Microsoft Photogrammetry, in: Fritsch, D. (Ed.), *Proceedings of the Photogrammetric Week 2007*, Stuttgart. pp. 137–145.
- Hebel, M., Stilla, U., 2008. Pre-classification of points and segmentation of urban objects by scan line analysis of airborne LiDAR data, in: *International Archives of the Photogrammetry, Remote Sensing and Spatial Information Sciences*, pp. 105–110.
- Hebel, M., Stilla, U., 2010. LiDAR-supported navigation of UAVs over urban areas. *Surveying and Land Information Science, Journal of the American Congress on Surveying and Mapping* 70, 139–149.
- Hebel, M., Stilla, U., 2012. Simultaneous calibration of ALS systems and alignment of multiview LiDAR scans of urban areas. *IEEE Transactions on Geoscience and Remote Sensing* 50, 2364–2379.
- Himmelsbach, M., Müller, A., Lüttel, T., Wünsche, H.J., 2008. LiDAR-based 3D object perception, in: *Proceedings of the 1st International Workshop on Cognition for Technical Systems*, pp. 1–7.
- Hinz, S., 2004. Automatic object extraction for change detection and GIS update, in: *International Archives of Photogrammetry, Remote Sensing and Spatial Geoinformation Sciences*, pp. 277–284.
- Hommel, M., 2009. Verification of a building damage analysis and extension to surroundings of reference buildings, in: *International Archives of the Photogrammetry, Remote Sensing and Spatial Information Sciences*, pp. 18–23.
- Hornung, A., Wurm, K.M., Bennewitz, M., Stachniss, C., Burgard, W., 2013. OctoMap: An efficient probabilistic 3D mapping framework based on octrees. *Autonomous Robots* 34, 189–206.
- Leberl, F., Meixner, P., Wendel, A., Irschara, A., 2012. Automated photogrammetry for three-dimensional models of urban spaces. *Optical Engineering* 51, 1–12.
- Matikainen, L., Hyypä, J., Ahokas, E., Markelin, L., Kaartinen, H., 2010. Automatic detection of buildings and changes in buildings for updating of maps. *Remote Sensing* 2, 1217–1248.
- Moras, J., Cherfaoui, V., Bonnifait, P., 2011. Moving objects detection by conflict analysis in evidential grids, in: *Proceedings of the IEEE Intelligent Vehicles Symposium IV’11*, pp. 1122–1127.
- Moravec, H., Elfes, A., 1985. High resolution maps from wide angle sonar, in: *Proceedings of the IEEE International Conference on Robotics and Automation*, pp. 116–121.
- Murakami, H., Nakagawa, K., Hasegawa, H., Shibata, T., Iwanami, E., 1999. Change detection of buildings using an airborne laser scanner. *ISPRS Journal of Photogrammetry and Remote Sensing* 54, 148–152.
- Pellenz, J., Paulus, D., 2008. Mapping and map scoring at the RoboCupRescue competition, in: *Quantitative Performance Evaluation of Navigation Solutions for Mobile Robots*, pp. 1–12.
- Puente, E., Moreno, L., Salichs, M., Gachet, D., 1991. Analysis of data fusion methods in certainty grids - application to collision danger monitoring, in: *Proceedings of the IEEE International*

- Conference on Industrial Electronics, Control and Instrumentation, pp. 1133–1137.
- Reitberger, J., Schnörr, C., Krzystek, P., Stilla, U., 2009. 3D segmentation of single trees exploiting full waveform LiDAR data. *ISPRS Journal of Photogrammetry and Remote Sensing* 64, 561–574.
- Rottensteiner, F., Sohn, G., Gerke, M., Wegner, J.D., 2013. ISPRS test project on urban classification and 3D building reconstruction, in: *Commission III - Photogrammetric Computer Vision and Image Analysis, Working Group III/4 - 3D Scene Analysis*, pp. 1–17.
- Rottensteiner, F., Trinder, J., Clode, S., Kubik, K., Lovell, B.C., 2004. Building detection by Dempster-Shafer fusion of LiDAR data and multispectral aerial imagery, in: *17th International Conference on Pattern Recognition, ICPR*, pp. 339–342.
- Rutzinger, M., Rüb, B., Höfle, B., Vetter, M., 2010. Change detection of building footprints from airborne laser scanning acquired in short time intervals, in: *International Archives of Photogrammetry, Remote Sensing and Spatial Information Sciences*, pp. 475–480.
- Schatz, V., 2008. Synchronised data acquisition for sensor data fusion in aerial surveying, in: *Proceedings of the 11th International Conference on Information Fusion*, pp. 1125–1130.
- Schenk, T., 2001. Modeling and analyzing systematic errors in airborne laser scanners. Technical Report. The Ohio State University.
- Schmitt, M., Stilla, U., 2011. Fusion of airborne multi-aspect InSAR data by simultaneous backward geocoding, in: *Joint Urban Remote Sensing Event (JURSE)*, pp. 53–56.
- Schulz, K.R., Scherbarth, S., Fabry, U., 2002. HELLAS: Obstacle warning system for helicopters, in: *Laser Radar Technology and Applications VII, Proceedings of the International Society for Optical Engineering* 4723, pp. 1–8.
- Shafer, G., 1976. *A Mathematical Theory of Evidence*. Technical Report. Princeton University.
- Stilla, U., Jutzi, B., 2009. Chapter 7: Waveform analysis for small-footprint pulsed laser systems. *Topographic Laser Ranging and Scanning: Principles and Processing* Shan J, Toth C, eds. CRC Press/Taylor & Francis Group, 215–234.
- Stilla, U., Sörgel, U., Thönnessen, U., 2003. Potential and limits of InSAR data for building reconstruction in built-up areas. *ISPRS Journal of Photogrammetry and Remote Sensing* 58, 113–123.
- Thrun, S., 1998. Learning metric-topological maps for indoor mobile robot navigation. *Artificial Intelligence* 99, 21–71.
- Tuttas, S., Stilla, U., 2012. Reconstruction of rectangular windows in multi-looking oblique view ALS data, in: *ISPRS Annals of Photogrammetry, Remote Sensing and Spatial Information Sciences*, pp. 317–322.
- Vögtle, T., Steinle, E., 2004. Detection and recognition of changes in building geometry derived from multitemporal laserscanning data, in: *International Archives of the Photogrammetry, Remote Sensing and Spatial Information Sciences*, pp. 428–433.
- Yao, W., Hinz, S., Stilla, U., 2011. Extraction and motion estimation of vehicles in single-pass airborne LiDAR data towards urban traffic analysis. *ISPRS Journal of Photogrammetry and Remote Sensing* 66, 260–271.
- Yapo, T.C., Steward, C.V., Radke, R.J., 2008. A probabilistic representation of LiDAR range data for efficient 3D object detection, in: *IEEE Conference on Computer Vision and Pattern Recognition, Workshop CVPRW'08*, pp. 1–8.
- Zou, Y., Ho, Y.K., Chua, C.S., Zhou, X.W., 2000. Multi-ultrasonic sensor fusion for mobile robots, in: *Proceedings of the IEEE Intelligent Vehicles Symposium*, pp. 387–391.